High-performance axicon lenses based on high-contrast, multilayer gratings

Sage Doshay, David Sell, Jianji Yang, Rui Yang, and Jonathan A. Fan

Citation: APL Photonics **3**, 011302 (2018); doi: 10.1063/1.5009760
View online: https://doi.org/10.1063/1.5009760
View Table of Contents: http://aip.scitation.org/toc/app/3/1
Published by the American Institute of Physics

High-performance axicon lenses based on high-contrast, multilayer gratings

Sage Doshay,[1] David Sell,[1] Jianji Yang,[2] Rui Yang,[2] and Jonathan A. Fan[2,a]
[1]*Department of Applied Physics, Stanford University, Stanford, California 94305, USA*
[2]*Department of Electrical Engineering, Stanford University, Stanford, California 94305, USA*

(Received 19 October 2017; accepted 22 December 2017; published online 16 January 2018)

Axicon lenses are versatile optical elements that can convert Gaussian beams to Bessel-like beams. In this letter, we demonstrate that axicons operating with high efficiencies and at large angles can be produced using high-contrast, multilayer gratings made from silicon. Efficient beam deflection of incident monochromatic light is enabled by higher-order optical modes in the silicon structure. Compared to diffractive devices made from low-contrast materials such as silicon dioxide, our multilayer devices have a relatively low spatial profile, reducing shadowing effects and enabling high efficiencies at large deflection angles. In addition, the feature sizes of these structures are relatively large, making the fabrication of near-infrared devices accessible with conventional optical lithography. Experimental lenses with deflection angles as large as 40° display field profiles that agree well with theory. Our concept can be used to design optical elements that produce higher-order Bessel-like beams, and the combination of high-contrast materials with multilayer architectures will more generally enable new classes of diffractive photonic structures. https://doi.org/10.1063/1.5009760

Axicon lenses have broad utility due to their ability to produce Bessel-like beams, which focus light along a line, suppress diffraction, and are self-healing.[1,2] These unique properties have made axicons useful in many applications in biological imaging, such as optical coherence tomography[3,4] and light-sheet microscopy,[5] where the linear focusing and robustness of Bessel-like beams to scattering enable improvements in resolution and depth of field. They are also used in telescopes that require the simultaneous focusing of targets located at different depths.[2] The distant field of an axicon has a ring-shaped intensity distribution and is used in laser eye surgery[6] and the trapping of atoms, biological cells, and microscopic colloids.[7,8]

Conventional axicon lenses are conical prisms that bend light via refraction [Fig. 1(a)]. While these devices are commercially available, they are bulky, difficult to manufacture, operate only within the transparency window of the lens material, and cannot generalize to produce higher-order Bessel beam responses. Alternative concepts that bend light based on diffractive optics offer the possibility of thinner, lightweight form factors, with a relatively broad range of optical properties specified by the geometric design. One class of diffractive-based axicons utilizes continuous echelle profiles[9,10] [Fig. 1(b)] or discrete multilayer blazed profiles[11,12] [Fig. 1(c)] made from low dielectric contrast materials such as silicon dioxide. These devices generally contain relatively large feature sizes and operate with high efficiencies at small deflection angles. However, when the grating periods are near the operation wavelength and the deflection angles are large (i.e., the "resonance domain"), the device efficiencies decrease due to shadowing effects incurred by the physical topology of these grating structures.[13–15] Alternative device designs utilizing very high aspect ratio structures have been proposed to improve the performance of glass multilayer blazed grating structures operating in the resonance domain.[16,17] While these devices support enhanced efficiency, they

[a]Author to whom correspondence should be addressed: jonfan@stanford.edu

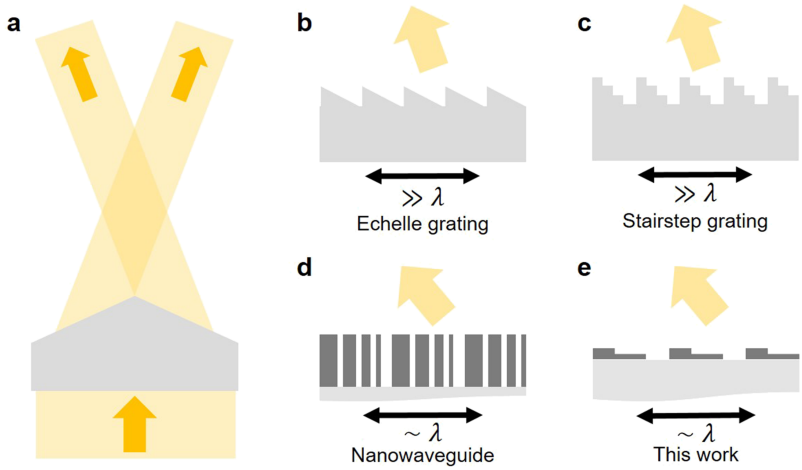

FIG. 1. Axicon operation and light diffraction methods. (a) A conventional bulk axicon, formed from a conical piece of glass, which bends light based on refraction. [(b)–(e)] The wavefront of an incident beam can also be specified by diffraction from a grating. There exist a broad range of grating designs, including (b) an echelle grating, (c) a stairstep-based diffraction grating etched in silicon dioxide, (d) a metasurface comprising high-aspect-ratio silicon nanowaveguides, and (e) low-aspect-ratio stairstep gratings etched in silicon, which are the subject of this work.

require patterning using electron-beam lithography, together with complicated, multi-step fabrication techniques.

Ultra-thin metasurfaces consisting of subwavelength-scale structures have also been proposed to push the performance limits of blazed gratings operating at visible and infrared wavelengths. Initial metasurface-based deflectors took the form of titanium dioxide waveguide ensembles,[18] and more recent advances in this field have incorporated a range of geometrically simple[19–23] and topologically complex[24–28] nanowaveguide and nanoresonator architectures [Fig. 1(d)]. These types of devices can efficiently deflect light to steep angles, but they require high-resolution nanopatterning based on electron beam or nanoimprint lithography.

In this letter, we show that high-contrast, multilayer gratings made from silicon [Fig. 1(e)] can be used to produce high-performance axicon lenses. Compared to existing diffraction-based axicons, our device architecture has two primary advantages. First, the grating structures in these devices have a very low spatial profile, which minimizes shadowing effects and allows for straightforward fabrication. Second, the feature sizes are relatively large. Lenses operating at near-infrared frequencies can be manufactured using conventional optical lithography, and any alignment-based fabrication errors will be significantly smaller than the key feature sizes. Our devices are conceptually distinct from single- and multi-layer silicon blazed gratings used in X-ray optics, which are based on scalar diffraction and utilize structures with very high aspect ratios.[29,30] For this study, we focus on cylindrically symmetric devices containing two levels of patterned material that can produce zeroth-order Bessel-like beams from Gaussian input waves.

The individual grating periods of our devices are set by the desired deflection angle θ_{ax}, with the period being $\lambda_{operation}/\sin(\theta_{ax})$, and contain a single silicon structure with a stairstep cross section on a fused silica substrate. These layouts consist of an upper, narrow rectangular section on top of and flush with the edge of a lower, wider rectangular section (see Fig. 1(e) for a schematic). To identify precise geometric parameters that enable efficient directional scattering for normally incident, monochromatic light, we parametrically sweep the total device thickness, the relative widths and thicknesses of each rectangular section, and the relative positions of the rectangular sections. In this process, we simulate structures in periodic arrays as linear gratings, using the rigorous coupled-wave analysis software package Reticolo,[31] and track the deflection efficiencies. The highest-efficiency grating structures calculated to deflect light to 15-, 20-, 30-, and 40-degree angles all comprise two 125 nm-thick layers of polycrystalline silicon on a silica substrate, and they possess the following device parameters. For the 15-degree deflection device, the period is 3.43 μm, the width of the lower

layer is 2.47 μm, and the width of the upper layer is 1.21 μm. For the 20-degree deflection device, the period is 2.6 μm, the width of the lower layer is 1.66 μm, and the width of the upper layer is 0.66 μm. For the 30-degree deflection device, the period is 1.78 μm, the width of the lower layer is 1.07 μm, and the width of the upper layer is 0.39 μm. For the 40-degree deflection device, the period is 1.38 μm, the width of the lower layer is 0.84 μm, and the width of the upper layer is 0.42 μm.

The calculated efficiencies for these high-efficiency grating structures are presented in Figs. 2(a) and 2(d) for TE-polarized incident light and TM-polarized incident light, respectively. In all cases, the absolute efficiencies, defined as the fraction of incident light diffracted to the desired deflection angle, and the relative efficiencies, defined as the fraction of transmitted light diffracted to the desired deflection angle, are reasonably high. In addition, the phase delay of the deflected beam is the same for TE and TM incident polarizations, which is critical for making functioning circularly symmetric devices. Interestingly, larger-angle devices possess relatively higher efficiencies. This is due to the reduced number of total diffraction channels available for scattering as the period of the grating decreases.

Full-wave electromagnetic simulations indicate that the high efficiencies observed in our blazed gratings originate from the ability of individual stairstep structures to scatter radiation in a directional manner. The scattering profiles of individual structures play a prominent role in our devices because the separation distances between scattering elements are relatively large, minimizing coupling between structures. As such, the collective responses of stairstep structures in our devices are determined by the constructive interference of the scattering profiles from individual structures. The total scattered field profiles for TE- and TM-polarized waves normally incident on an individual structure, from a grating designed for a 30-degree deflection angle, are plotted in Figs. 2(b) and 2(e), respectively. The asymmetric field profile is clearly visible and arises due to the asymmetric stairstep geometry. An examination of the field profiles within the silicon structures indicates coupling into higher-order modes, which arises from the high dielectric contrast featured in these relatively large-scale, low-profile structures. When these stairstep structures are stitched together into periodic arrays, the

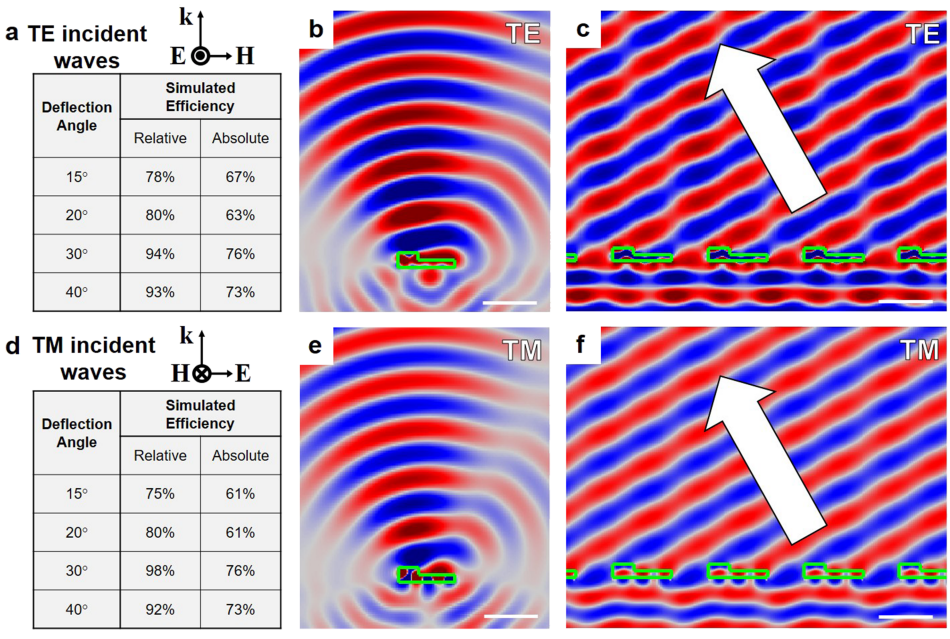

Deflection Angle	Simulated Efficiency	
	Relative	Absolute
15°	78%	67%
20°	80%	63%
30°	94%	76%
40°	93%	73%

Deflection Angle	Simulated Efficiency	
	Relative	Absolute
15°	75%	61%
20°	80%	61%
30°	98%	76%
40°	92%	73%

FIG. 2. Simulated deflection efficiencies and field profiles of stairstep silicon gratings on a glass substrate. [(a) and (d)] Simulated efficiencies of axicons operating at a range of deflection angles, for (a) TE and (d) TM incident polarizations. [(b) and (e)] Field profiles of an individual stairstep antenna, showing directional scattering and complex mode dynamics within the antenna, for (b) TE and (e) TM incident polarizations. [(c) and (f)] Field profiles of a periodic array of the same antenna, showing strongly angular scattering, for (c) TE and (f) TM polarizations. The antennas and gratings in (b), (c), (e), and (f) are designed for 30-degree deflection and a wavelength of 890 nm. Scale bars: 1 μm.

constructively interfering scattered fields produce clear wavefronts propagating toward the desired deflection angle [Figs. 2(c) and 2(f)].

To experimentally analyze these axicon lenses, we fabricate devices operating at a wavelength of 890 nm with deflection angles of 20°, 30°, and 40°. A summary of our fabrication process is in Fig. 3(a). Our first step is to grow 250 nm of polycrystalline silicon (p-Si) via chemical vapor deposition on both fused silica substrates and thermally oxidized silicon substrates. The films deposited on oxidized silicon substrates are used to characterize film thickness via ellipsometry and to calibrate etch rates. We then process the p-Si layer in two sequential patterning and etching steps to define the stairstep structures. The first lithography and etch process is used to define a section containing the upper rectangular section, and the etch depth is specified to be the thickness of this section. The second lithography step defines the complete stairstep structures, and etching is performed down to the silica substrate surface. We perform photolithography using an ASML PAS 5500/60 reducing stepper, which automates the alignment procedure between the two patterning steps. Images of a representative 20-degree deflection axicon are presented in Figs. 3(b)–3(d). The final device is 2 mm wide [Fig. 3(b), inset], and a low resolution scanning electron microscopy (SEM) image of the center of the axicon [Fig. 3(b)] shows clear cylindrical symmetry. High-resolution [Fig. 3(c)] and cross-sectional [Fig. 3(d)] views of the device indicate that the etching process produces smooth, vertical sidewalls and that the first etch step precisely stops at the top surfaces of the lower rectangular sections of the stairstep structures.

To optically characterize our axicons, we collimate and spatially filter unpolarized light from a Fianium white light laser, coupled to a monochrometer, and illuminate an individual device at its designed operating wavelength of 890 nm. The profile of the transmitted beam is imaged using a 50× Mitutoyo near-infrared objective (NA = 0.65), coupled to a 200 mm focal length tube lens and an Andor sCMOS camera. The position between the axicon and imaging train is tuned by mounting the device on a linear translation stage. Figures 4(a)–4(c) show transmitted intensity profiles for devices with deflection angles of 20°, 30°, and 40°, measured at the focal distance at which power in the central lobe is experimentally measured to be maximal. These profiles clearly demonstrate the characteristics of a zeroth-order Bessel-like beam, with a strong central peak surrounded by concentric rings of diminishing intensity. The intensities of the rings are generally isotropic, which indicates that the two patterning steps are well-aligned. The slight asymmetries in the field profiles of the 40-degree axicon are due to slight patterning misalignment in this particular device. To further analyze these field profiles, we compare them with those obtained via a full-field propagation calculation for an ideal axicon lenses supporting a linear radial phase delay at $z = 0$, $E(r, 0) = E_{\text{profile}}(r)e^{ikr\sin(\theta_{\text{ax}})}$. Experimental and theoretical plots of the field intensities along the axial cross section measured in Figs. 4(a)–4(c), plotted in Figs. 4(d)–4(f), show good agreement, especially in the dimensions of the Bessel-like beam rings. As Bessel beams are non-diffracting, these dimensions remain constant as the beam propagates. The experimental central peak beam radius is approximately 1 μm, 0.75 μm, and 0.5 μm, for the 20-, 30-, and 40-degree deflection axicons, respectively. The intensity deviations between the measured and simulated profiles for the 40-degree axicon, where the measured intensity

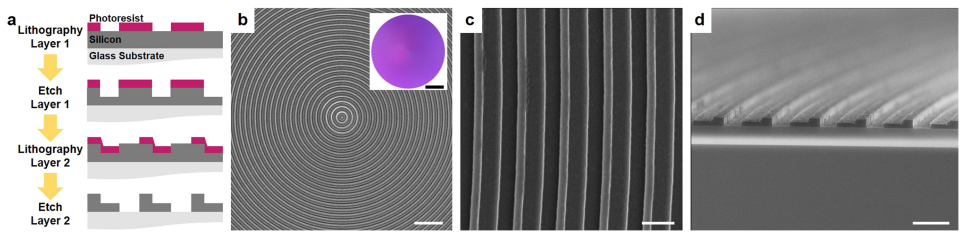

FIG. 3. Fabrication process and SEM images of axicon devices. (a) Summary of the silicon grating fabrication process. Two rounds of aligned lithography, each followed by etching, define the two-layer structures. (b) Low magnification SEM image of the 20-degree axicon designed to operate at 890 nm. Scale bar: 20 μm. Inset: optical image of the entire axicon lens. Scale bar: 0.5 mm. (c) High magnification SEM image of the rings of the 20-degree deflection axicon. Scale bar: 1 μm. (d) Cross-sectional SEM image of a cleaved 20-degree deflection axicon, showing the L-shape profile of each constituent stairstep structure. Scale bar: 2 μm.

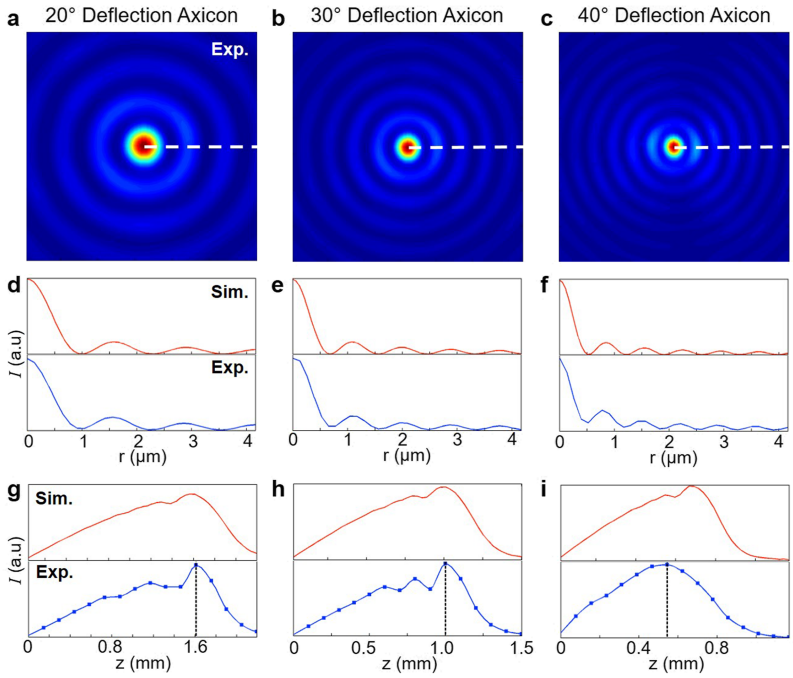

FIG. 4. Experimental characterization and simulated field profiles of silicon stairstep axicons. [(a)–(c)] Experimental transmitted intensity profiles for 20-, 30-, and 40-degree axicons, respectively. Measurements are taken at the distance with the highest experimental central peak intensity, demarcated in parts (g)–(i) by dashed vertical lines. [(d)–(f)] Simulated and experimental radial intensity values along the dashed horizontal lines shown in parts (a)–(c). [(g)–(i)] Simulated and experimental measurements of the intensity of the central peak as a function of distance from the lens. In all cases, experimental measurements match well with full-field simulations.

does not drop entirely to zero between the concentric rings of the Bessel-like beam, are due to polarization effects described in Ref. 32, which become more pronounced at higher angles of deflection.

A significant feature of axicons is that light focuses not to a point but to a line. This characteristic is visualized in the schematic in Fig. 1(a), where we can see that the Bessel-like beam forms from constructive interference occurring over a long path length (demarcated by the diamond-like area). Along the length of this focal line, the intensity increases up to $L_{\text{focal}} = R_{\text{ax}}/\tan(\theta_{\text{ax}})$, where R_{ax} is the radius of either the axicon or the illuminating beam, whichever is smaller, after which the intensity drops rapidly to zero.[33] Our fabricated axicons are 2 mm in diameter, and the experimental illuminating light has a beam waist of 1.5 mm. For each of our axicon lenses, we experimentally characterize the intensity of the central lobe as a function of focal distance and plot the results in Figs. 4(g)–4(i). We also calculate and plot the intensity of the central lobe for different focal distances via full-field simulations, using the measured profile of the incident beam in these calculations. These theoretical and experimental plots show good agreement, not only in the general intensity trends and in L_{focal} but also in the detailed dips present just before L_{focal}, which are a function of the specifics of the input beam. The deviation between the theoretical and experimental curves in the 40° device is due to the fact that the length scales in this particular structure are at the resolution limits of our lithographic patterning tool. These fabrication errors can be improved by the use of higher-resolution lithography tools.

In summary, we have shown that low-profile, multilayer silicon elements serve as effective directional scatterers for a broad range of scattering angles, making them suitable building blocks in diffractive-based axicon lenses. Devices operating at near-infrared wavelengths can be patterned using conventional photolithography, making the manufacturing of large-area devices straightforward and accessible. While our focus in this study is on cylindrically symmetric systems, our concepts can readily generalize to devices with broken cylindrical symmetry, which can convert Gaussian beams

to higher-order Bessel beams.[34,35] We anticipate that the scattering properties of our silicon elements can be further improved by incorporating overhangs and additional layers, which would involve the introduction of improved multilayer patterning and etching schema.[16,36] More generally, we envision that high-contrast elements with feature sizes accessible by photolithography can serve as a general pathway toward effective wavefront engineering in near-infrared and visible wavelength photonic devices.

The samples in this study were fabricated at the Stanford Nanofabrication Facility and the Stanford Nano Shared Facility. This work was supported by the Office of Naval Research under Award No. N00014-16-1-2630 and the Alfred P. Sloan Foundation. S.D. was supported by the Department of Defense through the National Defense Science and Engineering Graduate Fellowship Program. D.S. was supported by the National Science Foundation (NSF) through the NSF Graduate Research Fellowship.

[1] J. H. McLeod, J. Opt. Soc. Am. **44**(8), 592–597 (1954).
[2] J. H. McLeod, J. Opt. Soc. Am. **50**(2), 166–169 (1960).
[3] Z. Ding, H. Ren, Y. Zhao, J. S. Nelson, and Z. Chen, Opt. Lett. **27**(4), 243–245 (2002).
[4] K. S. Lee and J. P. Rolland, Opt. Lett. **33**(15), 1696–1698 (2008).
[5] R. M. Power and J. Huisker, Nat. Methods **14**, 360–373 (2017).
[6] O. Ren and R. Birngruber, IEEE J. Quantum Electron. **26**(12), 2305–2308 (1990).
[7] S. Kulin, S. Aubin, S. Christe, B. Peker, S. L. Rolston, and L. A. Orozco, J. Opt. B: Quantum Semiclassical Opt. **3**, 353–357 (2001).
[8] Y. Z. Yoon and P. Cicuta, Opt. Express **18**(7), 7076–7084 (2010).
[9] I. Golub, Opt. Lett. **31**(12), 1890–1892 (2006).
[10] K. Gourley, I. Golub, and B. Chebbi, Appl. Opt. **50**(3), 303–306 (2011).
[11] M. B. Fleming and M. C. Hutley, Appl. Opt. **36**(20), 4635–4643 (1997).
[12] L. Niggl, T. Lanzl, and M. Maier, J. Opt. Soc. Am. A **14**(1), 27–33 (1997).
[13] G. J. Swanson, MIT Technical Report 914, 1989.
[14] E. Loewen and E. Popov, *Diffraction Gratings and Applications* (Marcel Dekker, Inc., New York, NY, 1997).
[15] O. Sandfuchs, R. Brunner, D. Pätz, S. Sinzinger, and J. Ruoff, Opt. Lett. **31**(24), 3638–3640 (2006).
[16] M. Oliva, T. Harzendorf, D. Michaelis, U. D. Zeitner, and A. Tünnermann, Opt. Express **19**(15), 14735–14745 (2011).
[17] M. Oliva, D. Maichaelis, F. Fuchs, A. Tünnermann, and U. D. Zeitner, Appl. Phys. Lett. **102**, 203114 (2013).
[18] M.-S. L. Lee, P. Lalanne, and J.-C. Rodier, Opt. Lett. **25**(23), 1690–1692 (2000).
[19] D. Sell, J. Yang, S. Doshay, K. Zhang, and J. A. Fan, ACS Photonics **3**(10), 1919–1925 (2016).
[20] A. Y. Zhu, W. T. Chen, M. Khorasaninejad, J. Oh, A. Zaidi, I. Mishra, R. C. Devlin, and F. Capasso, APL Photonics **2**, 036103 (2017).
[21] L. Huang, X. Song, B. Reinke, T. Li, X. Li, J. Liu, S. Zhang, Y. Wang, and T. Zentgraf, ACS Photonics **4**(2), 338–346 (2017).
[22] S. Kruk, B. Hopkins, I. Kravchenko, A. Miroshnichenko, D. Neshev, and Y. Kivshar, APL Photonics **1**, 030801 (2016).
[23] D. Lin, P. Fan, E. Hasman, and M. L. Brongersma, Science **345**(6194), 298–302 (2014).
[24] D. Sell, J. Yang, S. Doshay, R. Yang, and J. A. Fan, Nano Lett. **17**(6), 3752–3757 (2017).
[25] J. Yang, D. Sell, and J. A. Fan, "Freeform metagratings based on complex light scattering dynamics for extreme, high efficiency beam steering," Ann. Phys. (published online).
[26] D. Sell, J. Yang, S. Doshay, and J. A. Fan, Adv. Opt. Mater. **5**, 1700645 (2017).
[27] J. Yang and J. A. Fan, Opt. Lett. **42**(16), 3161–3164 (2017).
[28] J. Yang and J. A. Fan, Opt. Express **25**(20), 23899–23909 (2017).
[29] C. David, Microelectron. Eng. **53**, 677–680 (2000).
[30] C. David, B. Nöhammer, and E. Ziegler, Microelectron. Eng. **61-62**, 987–992 (2002).
[31] J. P. Hugonin and P. Lalanne, *Reticolo Software for Grating Analysis* (Institut d'Optique, Orsay, France, 2005).
[32] W. T. Chen, M. Khorasaninejad, A. Y. Zhu, J. Oh, R. C. Devlin, A. Zaidi, and F. Capasso. Light: Sci. Appl. **6**, e16259 (2017).
[33] Y. Wang, S. Yan, A. T. Friberg, D. Kuebel, and T. D. Visser, J. Opt. Soc. Am. A **34**(7), 1201–1211 (2017).
[34] T. Ohno and S. Miyanishi, Opt. Express **14**(13), 6285–6290 (2006).
[35] N. Jiménez, R. Picó, V. Sánchez-Morcillo, V. Romero-García, L. M. García-Raffi, and K. Staliunas, Phys. Rev. E **94**, 053004 (2016).
[36] R. Huber, J. Conrad, L. Schmitt, K. Hercker, J. Scheurer, and M. Weber, Microelectron. Eng. **67-68**, 410–416 (2003).